Title

High Extracellular K+ Skews T-Cell Differentiation Towards Tumour Promoting Th2 and Treg Subsets.

Authors

Wong, Brandon

Poh, Zhi

Wei, James

et al.

Publication Date

2024-12-09

DOI

10.1002/eji.202451440

Peer reviewed

European Journal of Immunology

WILEY-VCH

European Journal of Immunology
Basic • Clinical • Translational

RESEARCH ARTICLE OPEN ACCESS

Adaptive Immunity

High Extracellular K^+ Skews T-Cell Differentiation Towards Tumour Promoting Th2 and T_{reg} Subsets

Brandon Han Siang Wong[1,2] | Zhi Sheng Poh[1] | James Tan Chia Wei[1] | Kottaiswamy Amuthavalli[1] | Ying Swan Ho[3] | Shuwen Chen[3] | Shi Ya Mak[3] | Xuezhi Bi[3] | Richard D. Webster[4] | Vishalkumar G. Shelat[1,5] | K. George Chandy[1] | Navin Kumar Verma[1,6,7]

[1]Lee Kong Chian School of Medicine, Nanyang Technological University, Singapore, Singapore | [2]Interdisciplinary Graduate Programme, NTU Institute for Health Technologies (HealthTech NTU), Nanyang Technological University, Singapore, Singapore | [3]Bioprocessing Technology Institute, Agency for Science Technology and Research (A*STAR), Singapore | [4]School of Chemistry, Chemical Engineering and Biotechnology, Nanyang Technological University, Singapore, Singapore | [5]Department of General Surgery, Tan Tock Seng Hospital, Singapore | [6]National Skin Centre, Singapore | [7]Skin Research Institute of Singapore, Singapore

Correspondence: Navin Kumar Verma (nkverma@ntu.edu.sg)

Received: 6 August 2024 | **Revised:** 25 November 2024 | **Accepted:** 26 November 2024

Funding: This research was supported, in part, by the Singapore Ministry of Education (MOE) under its MOE Academic Research Fund (AcRF) Tier 2 Grant (MOE2017-T2-2-004), AcRF Tier 1 Grant (2020-T1-001-062) and the National Research Foundation Singapore under its Open Fund Large Collaborative Grant (OFLCG18May-0028) and administered by the Singapore Ministry of Health's National Medical Research Council (NMRC). Navin Kumar Verma was a recipient of these grants. Brandon Han Siang Wong and Zhi Sheng Poh are recipients of PhD fellowships from HealthTech NTU and Lee Kong Chian School of Medicine, Nanyang Technological University Singapore.

Keywords: immune suppression | metabolomics | T-cell exhaustion | T-lymphocytes

ABSTRACT

Potassium ions (K^+) released from dying necrotic tumour cells accumulate in the tumour microenvironment (TME) and increase the local K^+ concentration to 50 mM (high-$[K^+]_e$). Here, we demonstrate that high-$[K^+]_e$ decreases expression of the T-cell receptor subunits CD3ε and CD3ζ and co-stimulatory receptor CD28 and thereby dysregulates intracellular signal transduction cascades. High-$[K^+]_e$ also alters the metabolic profiles of T-cells, limiting the metabolism of glucose and glutamine, consistent with functional exhaustion. These changes skew T-cell differentiation, favouring Th2 and iT_{reg} subsets that promote tumour growth while restricting antitumour Th1 and Th17 subsets. Similar phenotypes were noted in T-cells present within the necrosis-prone core versus the outer zones of hepatocellular carcinoma (HCC)/colorectal carcinoma (CRC) tumours as analysed by GeoMx digital spatial profiling and flow-cytometry. Our results thus expand the understanding of the contribution of high-$[K^+]_e$ to the immunosuppressive milieu in the TME.

1 | Introduction

Therapies that boost antitumour T-cell-mediated immunity, including cellular engineering strategies, chimeric antigen receptor (CAR) T-cell therapy, adoptive cell therapies and immunotherapies, have emerged as promising treatments for diverse cancers. Yet, the clinical efficacy of such approaches remains limited to a small percentage of patients [1–3]. In part, this is because the tumour microenvironment (TME) weakens immune responses by infiltrating lymphocytes in multiple ways [4]. Therefore, there is an increasing interest to reveal associated immunosuppressive mechanisms.

Following encounter with specific antigens, T-cells activate, proliferate and differentiate into distinct effector and memory subsets. Complex signalling and metabolic cascades polarize

T-cells into T helper 1 (Th1), Th2, Th17 or induced regulatory (iT_{reg}) subsets that exhibit distinct phenotypes and functional activities. Th1 cells mediate antitumour responses and are associated with better prognosis in the majority of tumours, whereas Th17 cells contribute to tumour elimination. In contrast, Th2 cells negatively impact antitumour immunity and iT_{reg} subsets create a pro-tumorigenic microenvironment by dampening T-cell effector function. An increased number of Th2 cells in the TME is associated with enhanced aggressiveness of tumours [5, 6].

A complexity of elements in the TME influences the function of T-cells and their differentiation to antitumour versus pro-tumour subsets. One such factor is extracellular potassium ions ($[K^+]_e$) released by dying necrotic tumour cells, which accumulate in the TME. Laser-induced breakdown spectroscopy has revealed substantially higher amounts of K^+ at the tumour border in bone-invasive oral cancer compared to healthy bones [7]. $[K^+]_e$ concentrations in the TME (~50 mM, designated here as high-$[K^+]_e$) are about 10 times higher than concentrations in the serum (3.5–5 mM) [8]. Tumour-infiltrating lymphocytes (TILs) exposed to the high-$[K^+]_e$-rich tumour interstitial fluid accumulate K^+ intracellularly [8, 9]. The intracellular K^+ concentration is normally around 135–145 mM. Accumulation of K^+ in TILs raises the intracellular K^+ concentration above a critical threshold, termed the 'K^+ ionic-checkpoint', causing suppression of antitumour TIL function [8, 9]. Here, utilizing human peripheral blood and hepatocellular carcinoma (HCC) and colorectal carcinoma (CRC) tissue samples, we explored the impact of high-$[K^+]_e$ on T-cell signalling and effector function. We demonstrate that high-$[K^+]_e$ disrupts T-cell-mediated signals implicated in T-cell metabolism and skews the differentiation of T-cell towards subsets that favour tumour growth.

2 | Results

2.1 | High-$[K^+]_e$ Inhibits T-Cell Proliferation by Impeding T-Cell Receptor (TCR) Signalling

In a previous study, we reported that cells maintained viability under isotonic high-$[K^+]_e$ conditions, whereas hypertonic high-$[K^+]_e$ was cytotoxic to T-cells in culture [9]. Therefore, we used isotonic high-$[K^+]_e$ in all the experiments in the current study. Exposure to isotonic 50 mM high-$[K^+]_e$ significantly suppressed the proliferation of $CD4^+$ and $CD8^+$ T-cells following activation via TCR engagement (Figure 1A). High-$[K^+]_e$ also suppressed interferon-gamma (IFN-γ) production by T-cells (Figure S1). This inhibitory effect was specific to high-$[K^+]_e$, as replacing $[K^+]_e$ with a similar amount of an inert cation tetramethylammonium did not impact IFN-γ production (Figure S1).

We compared the effect of high-$[K^+]_e$ versus physiological 5 mM $[K^+]_e$ on intracellular molecules that transduce TCR-mediated signals (Figure 1B) to understand the immunosuppressive mechanisms. High-$[K^+]_e$ significantly enhanced phosphorylation of the Src family protein tyrosine kinase Lck at its negative-regulatory C-terminal tail (pLck-Y505) (Figure 1C). Because Y505 phosphorylation of Lck inhibits its catalytic activity [10], we examined downstream signalling proteins that are typically phosphorylated by Lck, namely, ZAP70 (TCR zeta-chain-associated protein kinase 70), LAT (linker for activation of T-cells) and PLCγ1 (phospholipase Cγ1). Phosphorylation of all three substrates was significantly reduced by high-$[K^+]_e$ (Figure 1C). Signalling molecules further downstream in the cascade (p38, ERK1/2 [extracellular signal-regulated kinase 1 and 2], JNK [Jun N-terminal kinase], PKCθ [protein kinase C theta] and c-Jun) were also inhibited by high-$[K^+]_e$ (Figure 1C). These results demonstrate that high-$[K^+]_e$ suppresses TCR-dependent signalling cascade that is required for T-cell effector function.

2.2 | High-$[K^+]_e$ Reduces TCR Subunits and Co-Stimulatory Molecules

Given the important roles that TCR subunits (CD3ζ, CD3ε) and co-stimulatory receptors (CD28, LFA-1, CD2 and ICOS) play in T-cell effector function, we assessed the effect of high-$[K^+]_e$ on the expression of these molecules following stimulation by TCR crosslinking. Exposure to high-$[K^+]_e$ reduced mRNA expression of both CD3ζ and CD3ε in activated T-cells (Figure S2A,B). Flow-cytometry analysis confirmed high-$[K^+]_e$-mediated reduction in the expression of CD3ζ and CD3ε subunits in activated $CD4^+$ as well as $CD8^+$ T-cells (Figure 2A,B). High-$[K^+]_e$ also suppressed activation-induced expression of the co-stimulatory receptor CD28 (Figure 2C, Figure S2C), but not LFA-1, CD2, and ICOS in either $CD4^+$ or $CD8^+$ T-cells (Figure S3).

Surface TCR subunits and co-receptors are rapidly internalized following stimulation and are either recycled to the cell surface or degraded in lysosomes [11]. To test if lysosomal degradation underlies high-$[K^+]_e$-mediated decrease in CD3ζ, CD3ε and CD28, we added a lysosomal inhibitor, chloroquine (20 μM), during TCR engagement. Chloroquine partially reversed the high-$[K^+]_e$-induced decrease in CD3ζ expression (Figure 2D, Figure S4A), suggesting that lysosomal degradation contributes to high-$[K^+]_e$-dependent reduction in CD3ζ expression. Of relevance, high-$[K^+]_e$ significantly upregulated mRNA expression of the lysosomal protein LAPTM5 (Figure S5A), which interacts specifically with CD3ζ and promotes its lysosomal degradation without affecting CD3ε, CD3δ or CD3γ [12, 13]. A LAPTM5-dependent lysosomal mechanism may contribute to downregulation of CD3ζ in high-$[K^+]_e$. Chloroquine did not prevent high-$[K^+]_e$-induced decrease in expression of CD3ε and CD28 (Figure 2E,F, Figure S4B,C), suggesting that lysosome-independent mechanisms underlie high-$[K^+]_e$-mediated downregulation of CD3ε and CD28.

2.3 | High-$[K^+]_e$ Drives T-Cells Into a State of Functional Exhaustion

We examined the effect of high-$[K^+]_e$ on the expression of T-cell inhibitory molecules following stimulation by TCR crosslinking. High-$[K^+]_e$ increased mRNA and protein expression of the inhibitory receptors PD-1 and LAG-3 in $CD4^+$ and $CD8^+$ T-cells (Figure 3A,B, Figure S5B,C). Among activated T-cell populations containing a mixture of $CD4^+$ and $CD8^+$ T-cells, high-$[K^+]_e$ augmented the proportions of $CD69^+$ (Figure 3C) and $CD69^+CD25^-$ T-cells (Figure S6A), with a proportionate decrease in $CD69^-CD25^+$ T-cells (Figure 3D). CD69 is a type II glycoprotein that facilitates tumour immune escape by causing T-cell exhaustion [14, 15]. $CD69^+CD25^-$ T-cells are known to

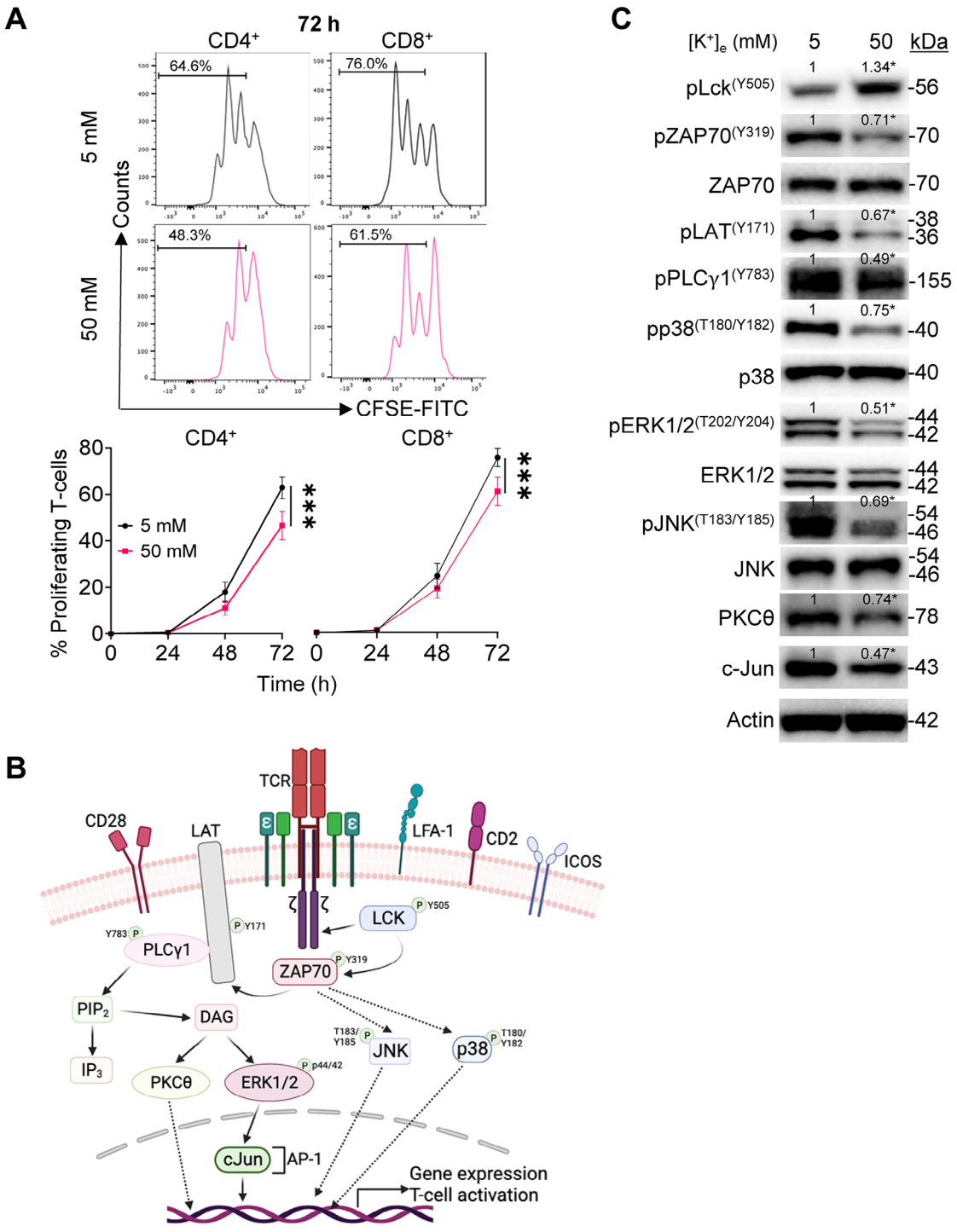

FIGURE 1 | Effect of high-$[K^+]_e$ on T-cell proliferation and TCR-mediated signalling. Human primary T-cells were activated via anti-CD3/28 in 5 or 50 mM $[K^+]_e$ medium. (A) Flow-cytometry histograms (upper panel) showing CFSE dilution of proliferating $CD4^+$ and $CD8^+$ T-cells 72 h post-activation from a single representative donor. Line graphs (lower panels) showing relative % of proliferating $CD4^+$ and $CD8^+$ T-cells measured at 24 h intervals over a period of 72 h. Each data point is mean ± SEM of six independent experiments using PBL T-cells from six different donors. (B) A schematic of the TCR-mediated signalling pathways. (C) After 72 h activation, cells were lysed and subsequently analysed by Western blotting to determine specific phosphorylation of TCR signalling proteins pLck (Y505), pZAP70 (Y319), pLAT (Y171), pPLCγ1 (Y783), pp38 (T180/Y182), pERK1/2 (T202/Y204) and pJNK (T183/Y185). Blots were also probed using antibodies against total proteins ZAP70, p38, ERK1/2, JNK, PKCθ and c-Jun, as well as actin, to confirm equal loading. Full-length blots are provided in the Supporting Information section. Densitometric analysis was performed relative to actin. Densitometry values indicated in the blots, normalized based on control T-cells activated in 5 mM $[K^+]_e$, are the means of at least three independent experiments using PBL T-cells from at least three different donors. *p* values were calculated using a two-tailed paired *t*-test (*$p < 0.05$; ***$p < 0.001$). CFSE, carboxy fluorescein succinimidyl ester.

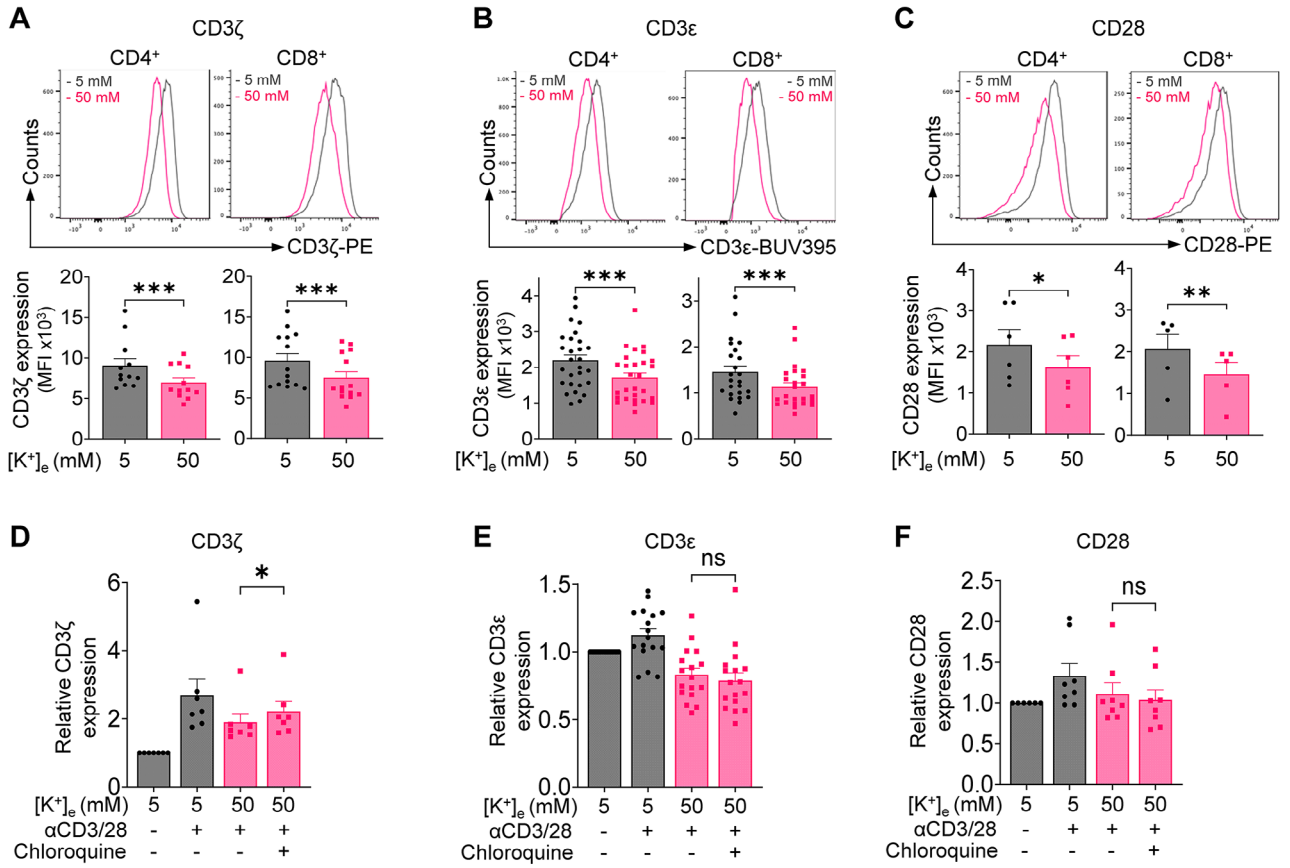

FIGURE 2 | Effect of high-$[K^+]_e$ on the expression of TCR subunits and the co-receptor CD28. Human primary T-cells were activated via anti-CD3/28 in 5 or 50 mM $[K^+]_e$ medium for 72 h. Cells were immuno-stained for (A) CD3ζ, (B) CD3ε and (C) CD28 and their expression levels in $CD4^+$ and $CD8^+$ T-cells were quantified using flow-cytometry. Histograms (upper panels) show fluorescence intensities corresponding to surface/intracellular expression of CD3ζ, CD3ε and CD28 72 h post-activation (a leftward shift indicates reduced expression) and bar graphs (lower panels) show their mean fluorescence intensities (MFIs). During the last 24 h of activation, cells were treated with 20 μM chloroquine and cellular expression levels of (D) CD3ζ, (E) CD3ε and (F) CD28 were quantified by flow-cytometry. Each data point represents PBL T-cells from an individual donor, and bar graphs show mean ± SEM. A two-tailed paired *t*-test (A–C) and one-way ANOVA (D–F) were used for statistical analysis of the results (*$p < 0.05$; **$p < 0.01$; ***$p < 0.001$; ns, non-significant).

exhibit suppressive regulatory function [16]. We next determined if these changes were in the $CD4^+$ and/or $CD8^+$ subsets. The $CD69^+CD25^-$ subset comprised about 3%–6% of both subsets when T-cells were activated in normal 5 mM $[K^+]_e$ but increased to 12% in the $CD4^+$ subset with no change in the $CD8^+$ subset when activation occurred in high-$[K^+]_e$ (Figure S6B). Notably, the majority (>70%) of $CD69^+CD25^-$ cells in both $CD4^+$ and $CD8^+$ subsets were $FOXP3^+$, suggesting their potential regulatory function. These effects of high-$[K^+]_e$ were concentration-dependent within the tested range of 12.5–80 mM $[K^+]_e$ (data not shown).

We reported earlier that high-$[K^+]_e$ reduced T-cell cytotoxicity of K562 cells [9]. In further support of functional exhaustion, we find that high-$[K^+]_e$ suppresses T-cell-mediated cytotoxicity of the breast cancer cell line MCF-7 (assessed by real-time impedance-based measurements) compared to physiological 5 mM $[K^+]_e$ (Figure 3E).

Mitochondrial dysfunction is a key feature of T-cell exhaustion [17]. Therefore, in addition to cytotoxicity assays, we performed mitochondrial assays to further confirm T-cell functional exhaustion. High-$[K^+]_e$ impaired T-cell mitochondrial function by lowering the mitochondrial membrane potential (Figure 3F), mitochondrial mass (Figure 3G) and the expression of proteins associated with mitochondrial dynamics, including dynamin-related protein 1 (DRP-1) and mitofusin-1 (MFN-1) (Figure 3H). Significantly, increased intracellular levels of reactive oxygen species were also noted in T-cells in the presence of high-$[K^+]_e$ (Figure 3I). Taken together, our data suggest that high-$[K^+]_e$ suppresses T-cell proliferation and cytokine production by decreasing critical signalling molecules, augmenting inhibitory proteins and impairing mitochondrial function, all of which are characteristics of functional T-cell exhaustion.

2.4 | High-$[K^+]_e$ Skews T-Cell Metabolic Pathways

T-cells utilize glucose and glutamine as nutrient sources during activation. Accordingly, glycolysis and glutaminolysis cooperatively control T-cell effector function (Figure 4A). Both metabolic processes are regulated by AMPKα (AMP-activated protein kinase catalytic subunit alpha), its substrate ACC (acetyl-CoA

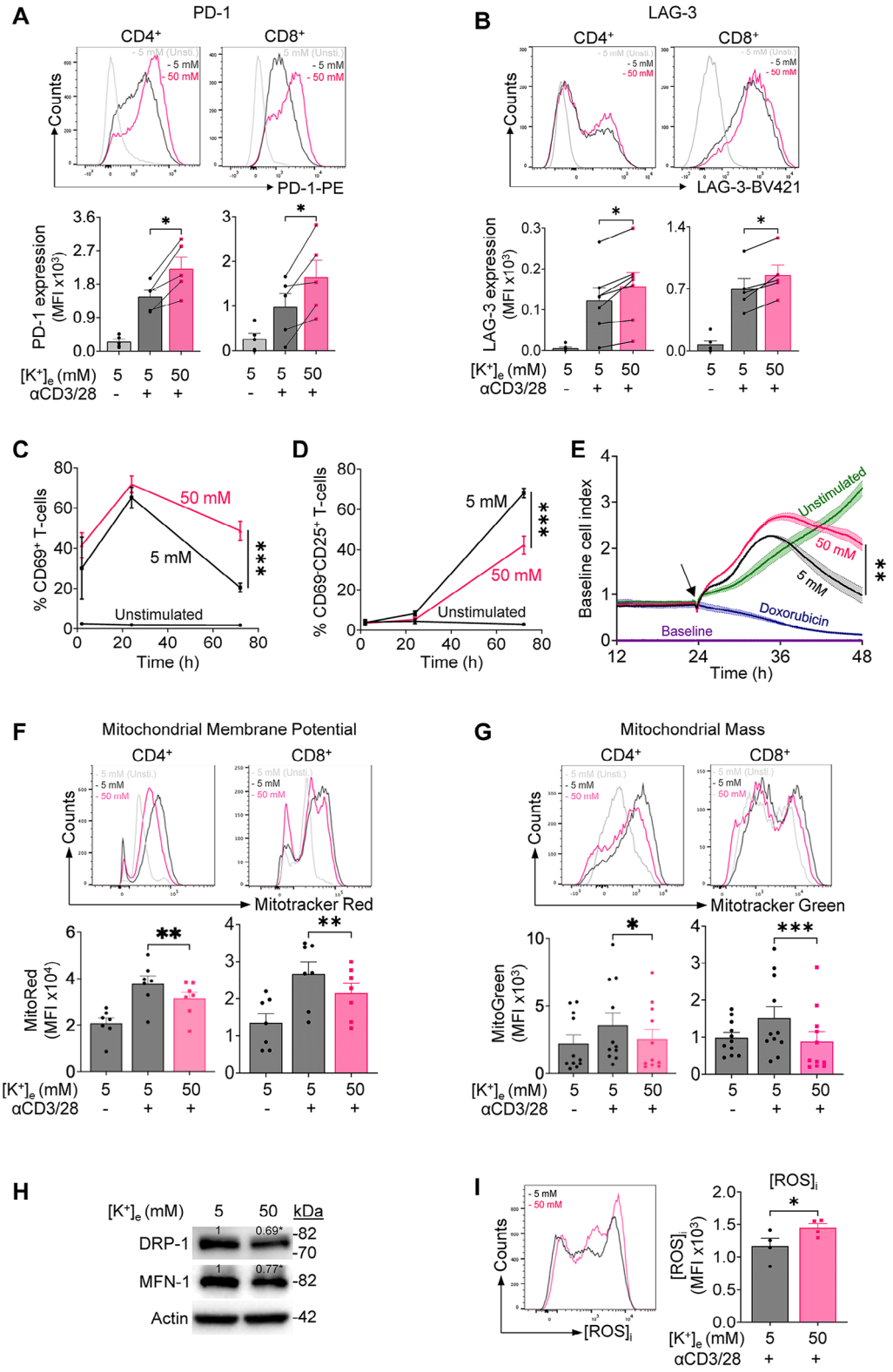

FIGURE 3 | Effect of high-$[K^+]_e$ on T-cell exhaustion markers. Human primary T-cells were activated via anti-CD3/28 crosslinking in 5 or 50 mM $[K^+]_e$ medium for 72 h. Cells were immuno-stained for (A) PD-1 and (B) LAG-3 and their expression levels in $CD4^+$ and $CD8^+$ T-cells were quantified using flow-cytometry. Histograms (upper panels) show fluorescence intensities corresponding to surface/intracellular expression of PD-1 and LAG-3 72 h post-activation (a rightward shift indicates increased expression) and bar graphs (lower panels) show their mean fluorescence intensities (MFIs). Cells were immuno-stained for CD69 and CD25 and relative % of (C) $CD69^+$ and (D) $CD69^-CD25^+$ T-cells was quantified by flow-cytometry at 2, 24 and 72 h post-activation. Each data point is mean ± SEM of four independent experiments using PBL T-cells from four different donors. (E) T-cell cytotoxicity killing of cultured MCF-7 breast cancer cells, monitored in real-time using xCELLigence RTCA system, for up to 24 h after co-culture. Arrow denotes the time-point at which either unstimulated (control) or activated T-cells (using 1 μg/mL anti-CD3 and 20 ng/mL IL-2) in 5 or 50 mM $[K^+]_e$ medium were added to the growing monolayer of MCF-7 cells. Doxorubicin (20 μM) was added to certain wells as a toxicity control. The baseline cell index line graph

carboxylase), and the transcription factor c-Myc [18]. High-$[K^+]_e$ reduced the phosphorylation of AMPKα and ACC and decreased mRNA and protein expression of c-Myc (Figure 4B, Figure S5D), implying that exposure to high-$[K^+]_e$ alters T-cell metabolic programming. A comparative non-targeted metabolomic profiling of T-cells activated under high-$[K^+]_e$ showed two distinct groups of metabolites separated by principal component analysis (Figure S7). We identified 28 metabolites that were significantly dysregulated in T-cells by high-$[K^+]_e$ (Figure 4C), particularly metabolic pathways involving glycerophospholipids/lipids and the TCA cycle (Figure 4D). Because dysregulated lipid pathway by extracellular $[K^+]_e$ has been highlighted in an earlier study [19], we focused on carbohydrate metabolism in the current investigation.

Glucose is transported into T-cells by glucose transporters, mainly GLUT1 and GLUT4, whereas transport of glutamine is by SLC38A1. In activated T-cells, high-$[K^+]_e$ decreased levels of mRNA and proteins for GLUT1, GLUT4 and SLC38A1 (Figure 4E, Figure S8A,B) and accordingly reduced the uptake of glucose and glutamine (Figure 4F, Figure S8C). Once inside T-cells, glucose and glutamine undergo glycolysis and glutaminolysis, respectively, and generate ATP that fuels T-cell effector function. High-$[K^+]_e$ decreased expression of key enzymes involved in glycolysis, hexokinase 2 (HK2, Figure 4G) and the alternative pentose phosphate pathway, glucose-6-phosphate dehydrogenase (G6PD; Figure 4H). Moreover, high-$[K^+]_e$ significantly decreased the expression of glutaminolysis-associated enzymes: glutaminase (GLS), glutamine synthetase (GS) and glutamate dehydrogenase 1 (GLUD1) (Figure 4I) that produce substrates to drive the TCA cycle and contribute to energy production in activated T-cells. Reduced mRNA and protein expression of key enzymes involved in TCA cycle, citrate synthase (CS) and fumarate hydratase were evidently observed (Figure 4J,K). These results suggest that high-$[K^+]_e$ induces functional exhaustion of T-cells by diminishing glycolysis and glutaminolysis.

To further substantiate the impact of high-$[K^+]_e$ in dysregulating T-cell carbohydrate metabolism in human cancer, we performed GeoMx digital spatial profiling of HCC/CRC tumour-infiltrated T-cells (Figure 5A). Dysregulated TCA cycle and TCR signalling were evident in T-cells that were infiltrated in the tumour core (necrotic and $[K^+]_e$-enriched region) compared to T-cells present in the peripheral (outer) zone of HCC/CRC tumour tissues (Figure 5B).

2.5 | High-$[K^+]_e$ Shifts the Balance of T-Cell Differentiation Towards Th2

Because T-cell differentiation is dependent on cellular metabolism [20–22], we investigated whether high-$[K^+]_e$-mediated changes in T-cell metabolism impact differentiation into various $CD4^+$ subsets (Figure 6A). We isolated T-cells from healthy donors' peripheral blood, stimulated via TCR engagement in the absence or presence of high-$[K^+]_e$ for 6 days, and measured the proportion of Th1, Th2, Th17 and iT_{reg} subsets. T-cell differentiation was allowed to progress in an unbiased manner with no agents (e.g., antibodies against cytokines or polarizing cytokines) added to skew differentiation along a particular lineage. Exposure to high-$[K^+]_e$ decreased the proportion of $CD4^+$ Th1 cells with a consequent increase in Th2 cells (Figure 6B, Figure S9). In support of this Th2 bias, high-$[K^+]_e$ decreased secretion of the Th1 cytokine IFN-γ and increased secretion of the Th2 cytokine IL-4 (Figure 6C). Furthermore, high-$[K^+]_e$ decreased the expression of T-bet, a master regulator of Th1 differentiation, and increased the expression of GATA3, a master regulator of Th2 differentiation (Figure 6D, Figure S10), along with transcriptional regulators of GATA3 (EGR1, JunB, c-MAF, and RBPJ; Figure 6E).

High-$[K^+]_e$ inhibited T-cell Th17 differentiation, reduced the expression of RORγt (a master regulator of Th17 differentiation) and the interleukin 17 receptor (IL-17R) and suppressed the secretion of the Th17-specific pro-inflammatory cytokine IL-17A (Figure 6F). In contrast, high-$[K^+]_e$ enhanced the proportion of $CD4^+$ iT_{reg} cells and augmented the expression of FOXP3 (Figure 6G, Figure S11) along with transcriptional regulators of FOXP3 (CTLA4, CD73, EOS, FOXO3, FOXO1, c-Rel; Figure 6H) that are responsible for T-cell differentiation into iT_{reg}.

To further substantiate the impact of high-$[K^+]_e$ in driving T-cell differentiation towards the Th2 and iT_{reg} subsets, T-cells present in the necrosis-prone tumour core were phenotyped and compared with T-cells present in the outer zone of HCC/CRC tumours (Figure 6I, Figure S12). Congruent with the above findings, we found a significant decrease in Th1 cells and an increase in Th2 cells in the core of HCC/CRC tumours compared to their periphery (Figure 6J).

We performed point biserial correlation analysis to assess the relationship between the relative percentages of Th1/Th2 subsets in the outer and core regions of the tumours. Analysis of the

represents three independent experiments that exhibited similar readouts. T-cells were stained with (F) MitoTracker Red CMXRos dye (MitoRed) to quantify mitochondrial membrane potential or (G) MitoTracker Green FM dye (MitoGreen) to quantify mitochondrial mass. Flow-cytometry histograms (upper panels) show fluorescence intensities corresponding to MitoRed and MitoGreen signals obtained from a single representative donor's T-cells (a leftward shift indicates reduced signals), and bar graphs (mean ± SEM, lower panels) show mean fluorescence intensities (MFIs) in $CD4^+$ and $CD8^+$ T-cells. (H) Cells were lysed and subsequently analysed by Western blotting for the expression of DRP-1 and MFN-1. Blots were probed with actin to confirm equal loading and densitometry values indicated in the blots, normalized based on control T-cells activated in 5 mM $[K^+]_e$, are the mean of at least three independent experiments using PBL T-cells from at least three different donors. Full-length blots are provided in the Supporting Information section. (I) T-cells activated in 5 or 50 mM $[K^+]_e$ medium for 72 h were stained with CellROX Deep Red reagent to quantify levels of intracellular reactive oxygen species ($[ROS]_i$) by flow-cytometry. Histograms show fluorescence intensities corresponding to CellROX Deep Red reagent signals obtained from a single representative donor's T-cells and bar graph (mean ± SEM) show MFI values. Each data point in bar graphs represents PBL T-cells from an individual donor. A two-tailed paired *t*-test (C–E, H, and I) and one-way ANOVA (A, B, F, and G) were used for statistical analysis of the results (*$p < 0.05$; **$p < 0.01$; ***$p < 0.001$). DRP-1, dynamin-related protein 1.

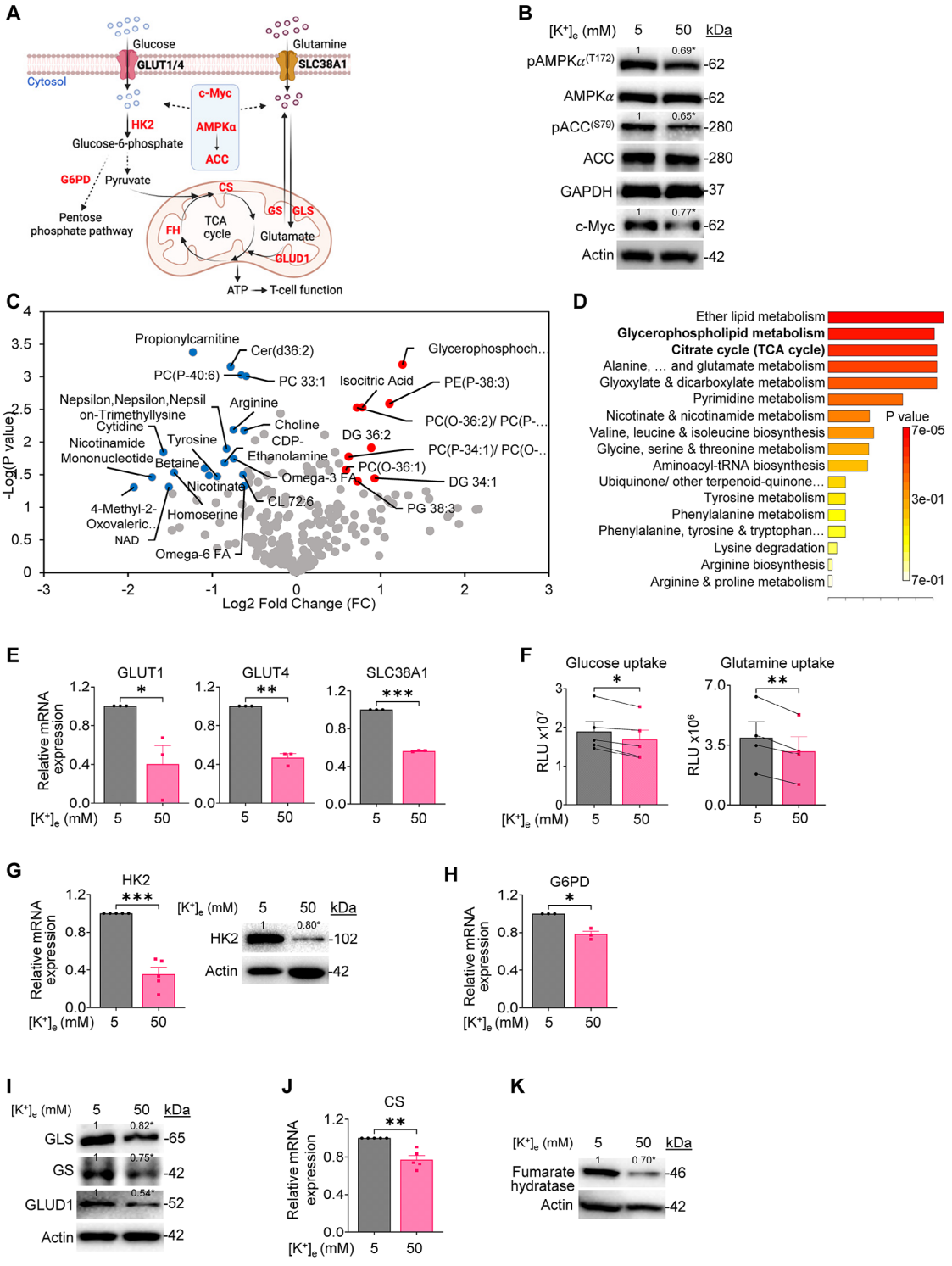

FIGURE 4 | Effect of high-$[K^+]_e$ on T-cell metabolomics and metabolomic pathways. (A) Schematic of glucose and glutamine metabolism and associated enzymes involved in regulating T-cell function. (B) Human PBL T-cells were activated via anti-CD3/28 in 5 or 50 mM $[K^+]_e$ medium, lysed after 24 h activation and subsequently analysed by Western blotting for the expression of pAMPKα (T172), pACC (S79) and c-Myc. Blots were also probed using antibodies against total proteins pAMPKα, ACC, GAPDH and actin to confirm equal loading. (C) Human PBL T-cells from four healthy donors ($n = 4$) were activated separately via anti-CD3/28 in 5 or 50 mM $[K^+]_e$ medium for 6 days. Metabolomic analysis was performed by mass spectrometry, and cellular metabolites exhibiting at least a 0.5-fold change in the upregulation (indicated in red dots) or downregulation (indicated in blue dots) due to exposure to high-$[K^+]_e$ are shown. (D) Summary of metabolic pathway enrichment analysis performed in MetaboAnalyst (Version 5.0., URL: https://www.metaboanalyst.ca). (E) After 24 h activation, expression levels of GLUT1, GLUT4 and SLC38A1 mRNA transcripts in T-cells were quantified by RT-qPCR. (F) After 24 h activation, cellular uptake of glucose and glutamine was quantified using bio-luminescence assays in terms of relative light units (RLUs). (G) After 24 h activation, expression levels of HK2 mRNA transcripts and protein were quantified by RT-qPCR and Western blotting, respectively. (H) After 24 h activation, expression levels of G6PD mRNA transcripts were quantified by RT-qPCR. (I) After 24 h activation, cells were

Th2 subset yielded a positive point biserial correlation coefficient (r_{pb}) of +0.23, which indicates an increase in the relative % of the Th2 subset towards the tumour core. In contrast, analysis of the Th1 subset yielded a negative r_{pb} value of −0.23 (Figure 6J), which indicates a decrease in the relative % of Th1 subset towards the tumour core. Significantly higher % of $FOXP3^+CD4^+$ T-cells was also noted in HCC/CRC tumours compared to peripheral blood obtained from healthy volunteers (Figure 6K). These results confirm that high-$[K^+]_e$ skews T-cell differentiation towards Th2 and iT_{reg}s, which would ultimately favour tumour immune escape.

3 | Discussion

The TME harbours increased $[K^+]_e$, adenosine, lactate, acidosis, phosphatidylserine, vascular endothelial growth factor and hypoxia. All these agents acting in concert depress the function of infiltrating T-cells and other immune cell types, ultimately impairing antitumour immune responses [4]. Of relevance to our study, the $[K^+]_e$ concentration in the TME is 10 times higher than in serum. Here, we show that high-$[K^+]_e$ limits the ability of T-cells to proliferate and transforms T-cells into a hyporesponsive state of exhaustion by disrupting TCR signals and dysregulating mitochondrial and metabolic function during the early stages of T-cell activation that ultimately skew T-cell differentiation towards suppressive Th2 and iT_{reg} subsets.

The overall activation state of T-cells and their ability to proliferate is vital in eliciting an optimal antitumour response [22–24]. A functionally active assembly of the TCR complex requires appropriate expression of all the TCR subunits, including the CD3ε and CD3ζ chains. CD28 provides a second signal, which is essential for the activation, effector function, and differentiation of T-cells [25–27]. High-$[K^+]_e$, through reduced expression of CD3ζ, CD3ε, and CD28, impaired TCR signalling cascades and dampened T-cell activation. The effects of high-$[K^+]_e$ on T-cell effector function were evident in the early stages of activation, as early as 24 h. High-$[K^+]_e$-mediated impairment of TCR signalling and dysregulation of T-cell mitochondrial and metabolic function also occurred during early stages of activation. These results suggest that changes occurring within the first 24–48 h skew T-cell differentiation (in vitro differentiation assay is 5- to 7-day duration) towards suppressive Th2 and iT_{reg} subsets.

The expression and recycling of T-cell surface receptors are regulated by multiple mechanisms, and proteolysis plays a key role [11]. Studies with the lysosomal inhibitor chrloroquine suggest that high-$[K^+]_e$-mediated decreased surface expression of CD3ζ in activated T-cells is partially dependent on lysosomal proteolysis. Notably, high-$[K^+]_e$ upregulates the lysosomal protein LAPTM5, which promotes lysosomal degradation of CD3ζ without affecting CD3ε, CD3δ or CD3γ [12, 13], suggesting that a LAPTM5-dependent lysosomal mechanism may contribute to downregulation of CD3ζ in high-$[K^+]_e$. Because chloroquine treatment did not prevent the high-$[K^+]_e$-driven reduction of CD3ε and CD28 expression, it is likely that lysosomal-independent mechanisms are operative. High-$[K^+]_e$ inhibits the ability of T-cells to produce IL-2 [9], which is required for CD28 expression [28]. PD-1, a known inhibitor of CD28 expression and TCR signalling [29, 30], is also upregulated by high-$[K^+]_e$. These mechanisms may contribute to the downregulation of CD28 in high-$[K^+]_e$. In summary, complex lysosomal-dependent and lysosomal-independent mechanisms contribute to the high-$[K^+]_e$-dependent decrease in CD3ζ, CD3ε and CD28.

High-$[K^+]_e$ upregulated the expression of inhibitory receptors, PD-1 and LAG3, which are important molecules causing T-cell exhaustion [31]. A recent study using mouse models of melanoma showed that both inhibitory receptors (PD-1 and LAG3) synergize in driving T-cell exhaustion and hindering antitumour immunity [32]. Moreover, combinatorial targeting of LAG-3 (by anti-LAG-3, relatlimab) and PD-1 (by anti-PD-1, nivolumab) showed enhanced efficacy in melanoma patients [33]. High-$[K^+]_e$ also decreased the uptake and metabolism of glucose and glutamine and impaired the activity of proteins controlling the T-cell metabolic program (AMPKα, c-Myc), leading to T-cell exhaustion. The altered metabolic profile skewed T-cell differentiation towards subsets (Th2 and iT_{reg}) that can promote tumour growth while decreasing subsets with antitumour potential (Th1, Th17).

CRISPR-Cas9-mediated disruption of the ATP1A1 gene that encodes Na^+/K^+ ATPase decreased intracellular K^+ in mouse and human $CD8^+$ T-cells [34], presumably by decreasing K^+ entry into the cells. Exit of K^+ from TILs is through two K^+ channels, $K_V1.3$ and $K_{Ca}3.1$ [35]. Both channels have been reported to be reduced in TILs due to hypoxia and acidosis in the TME and the action of inhibitory receptors [35]. Therefore, therapeutic approaches that modulate the entry and exit pathways of K^+ in TILs or buffer intracellular K^+ may optimize antitumour TIL function.

Precisely controlled signalling cascades, cellular metabolism and energy are important for T-cells to achieve optimal activation. We observed high-$[K^+]_e$-induced impairment in the activity of AMPKα and c-Myc, the two important proteins that control the T-cell metabolic program [36]. Although an impaired AMPKα activity would render T-cells incapable of generating sufficient ATP for their effector function, insufficient c-Myc expression would inhibit the expression of glucose and glutamine transporters needed by active T-cells for their glucose and glutamine uptake and energy production [37]. The impairment of glucose

lysed and subsequently analysed by Western blotting for the expression of GLS, GS and GLUD1. (J) After 24 h activation, expression levels of CS mRNA transcripts were quantified by RT-qPCR. (K) After 24 h activation, cells were lysed and subsequently analysed by Western blotting for the expression of fumarate hydratase. Densitometry values indicated in the blots (B, G, I, and K), normalized based on control T-cells activated in 5 mM $[K^+]_e$ relative to actin, are mean of at least three independent experiments using PBL T-cells from at least three different donors. Full-length blots are provided in the Supporting Information section. Each data point in the graphs represents PBL T-cells from an individual donor, and bar graphs show mean ± SEM. A two-tailed paired *t*-test was used for statistical analysis of the results (*$p < 0.05$; **$p < 0.01$; ***$p < 0.001$). CS, citrate synthase; GLS, glutaminase; GS, glutamine synthetase; GLUD1, glutamate dehydrogenase 1.

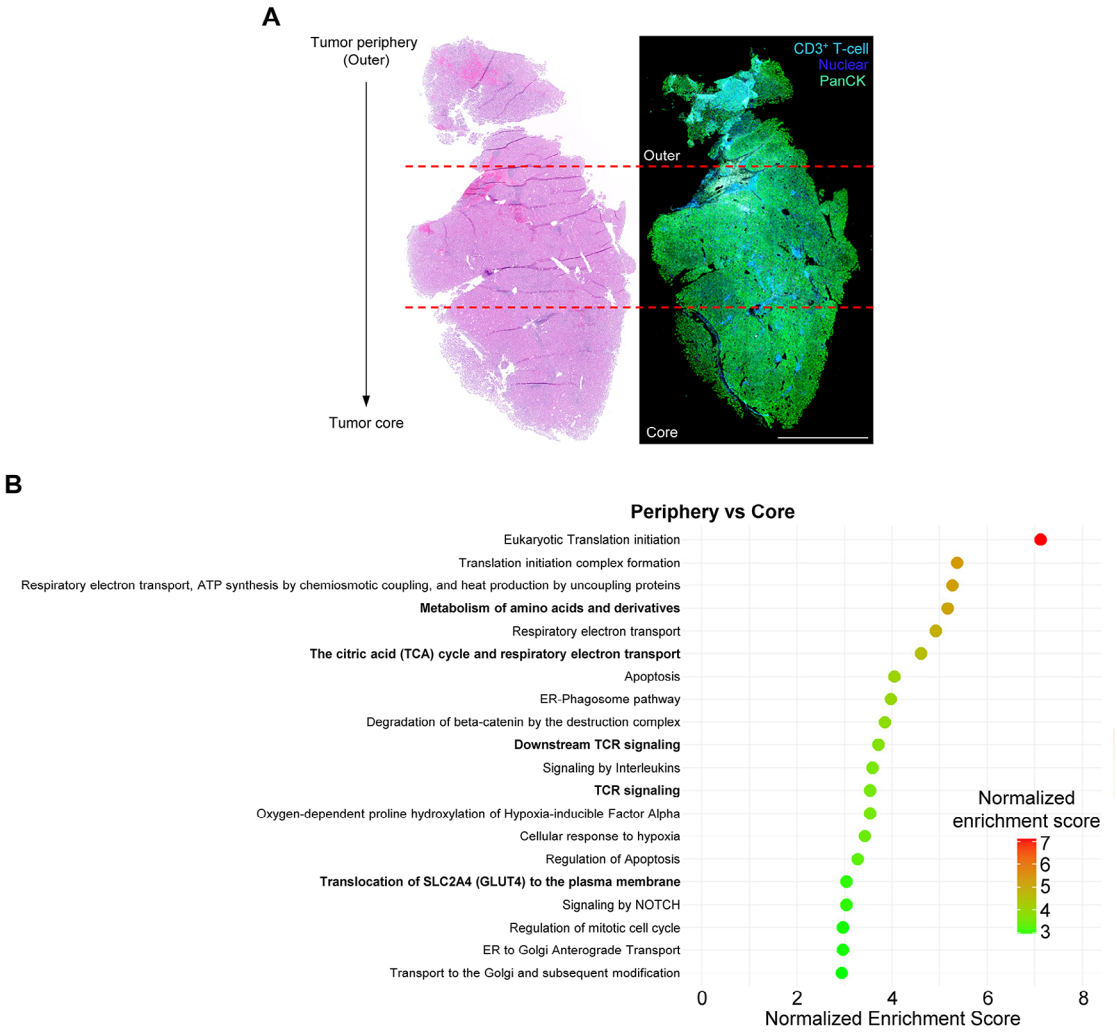

FIGURE 5 | Digital spatial profiling of T-cells between the tumour periphery and core of HCC/CRC tumours. (A) A representative schematic of the demarcation of the periphery (outer) and core zones of a tumour biopsy. HCC/CRC tumour ($n = 8$ patients) sections were stained for the following morphological markers: $CD3^+$ T-cells (cyan), nucleus (blue) and PanCK (green). Scale bar (white line) is 2.5 mm. (B) Bubble plot of the top 20 pathways based on genes with a log2 fold change of 0.5 with an adjusted p value of less than 0.05 that were identified in T-cells within the tumour core compared to T-cells within the tumour outer zones. *Note*: pathways highlighted in bold are in complementarity with our in vitro findings.

metabolism under high-$[K^+]_e$ conditions could explain T-cell exhaustion with increased differentiation towards the T_{reg} subsets [38]. Furthermore, the reduced glucose uptake mediated by high-$[K^+]_e$ can lead to caloric restriction and induce stemness-like phenotypes in T-cells [19]. High-$[K^+]_e$-induced impairment in CD28 expression may have further contributed to reduced Th1 differentiation.

Aside from glycolysis, the high-$[K^+]_e$-mediated perturbations in glutaminolysis could also reduce the relative % of Th1 and Th17 while promoting the generation of $FOXP3^+$ T_{reg} cells. Specifically, it could be attributed to the reduced levels of glutathione, which is a downstream byproduct of glutaminolysis. Because glutathione is an immunomodulatory antioxidant that favours Th1 response [39], high-$[K^+]_e$-mediated reduction of glutathione would contribute to increased Th2 differentiation, which has been associated with increased tumour proliferation [40]. Likewise, the decrease in AMPKα activity mediated by high-$[K^+]_e$ could have contributed to the increase in the IL-4/STAT6/GATA3 axis, driving T-cell differentiation towards the Th2 lineage [41]. Tumour-infiltrating T-cells are particularly prone to exposure to high-$[K^+]_e$ gradient from outer regions to the core region, as tumour core contains the highest number of dying/necrotic cells [35].

In conclusion, our investigation revealed that high-$[K^+]_e$ suppresses T-cell function, including its activation and proliferation, by hampering TCR-mediated signalling in conjunction with the dysregulation of co-stimulatory molecules. It is likely that high-$[K^+]_e$ impacts multiple pathways and signalling cascades (in addition to TCR) that favour Th2 and iT_{reg} differentiation and impair T-cell antitumour cytotoxicity. In the differentiation continuum, iT_{reg} cells are more similar to memory subsets than effector/Th1 subsets, and they exhibit unique metabolic behaviour. Our findings point towards a complex picture under $[K^+]_e$, with less T-bet/Th1 abundance, typically a pre-requisite for T-cell exhaustion. We propose that high-$[K^+]_e$-induced impairment in TCR signals and metabolic alteration in T-cells contribute

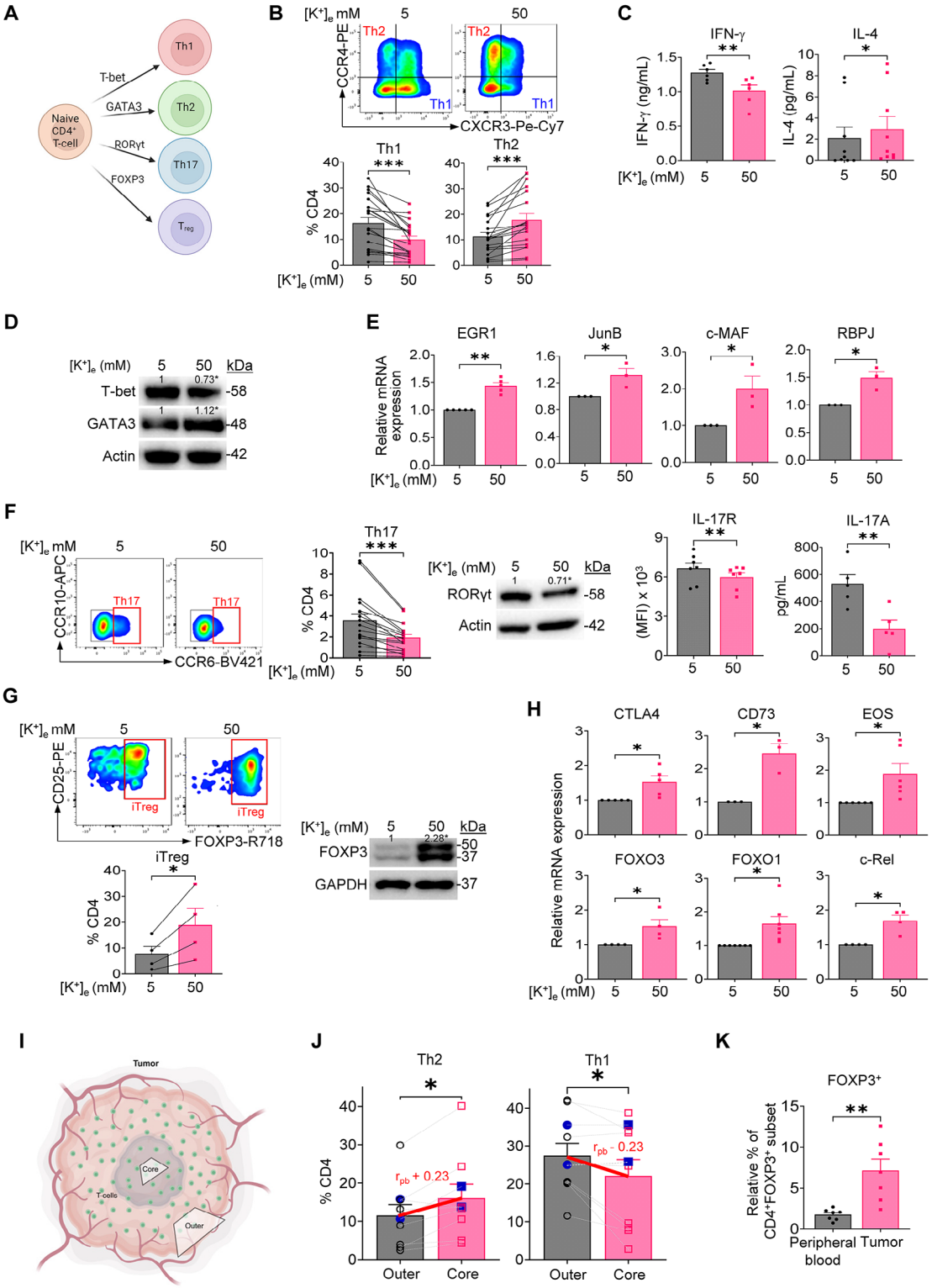

FIGURE 6 | Effect of high-$[K^+]_e$ on T-cell differentiation. (A) A schematic of T-cell polarization into various Th subsets—Th1, Th2, Th17 and T_{reg}. Human PBL T-cells were activated via anti-CD3/28 in 5 mM $[K^+]_e$ or 50 mM $[K^+]_e$ for 6 days. (B) Relative % of Th1 and Th2 subsets (relative to $CD4^+$ T-cells) was quantified by flow-cytometry. Pseudocolour plots (upper panel) display the relative population density of Th1 (bottom right quadrant) and Th2 (top left quadrant) cell populations 6-day post-activation, and bar graphs (lower panels) show their relative % among $CD4^+$ T-cells. (C) Secreted levels of IFN-γ and IL-4 by T-cells 6 days post-activation as determined by ELISA. (D) Activated T-cells in "B" were lysed and subsequently analysed by Western blotting for the expression of T-bet and GATA3. (E) Expression levels of EGR1, JunB, c-MAF, and RBPJ mRNA transcripts in activated T-cells were determined by RT-qPCR. (F) Relative % of Th17 population (relative to $CD4^+$ T-cells) was quantified by flow-cytometry (pseudocolor plots and the graph). Expression levels of RORγt were determined by Western immunoblotting, surface expression of IL-17R was quantified by flow-cytometry, and secreted levels of IL-17A were determined by ELISA. (G) Relative % of iTreg population (relative to $CD4^+$ T-cells) was quantified by flow-cytometry (pseudocolor plots and the graph). Cellular expression levels of FOXP3 were determined by Western blotting. (H) Expression levels of CTLA4, CD73,

to a weakened T-cell antitumour response in the TME. A therapeutic approach combining standard-of-care checkpoint inhibitors with approaches to decrease elevated intracellular K^+ may be beneficial.

4 | Materials and Methods

4.1 | Human Primary T-Cells and Tumour Tissues

Human blood buffy-coat samples from anonymized healthy volunteers were collected from Health Sciences Authority, Singapore. Peripheral blood lymphocyte (PBL) T-cells were isolated using density gradient centrifugation and cultured in RPMI 1640 supplemented with 10% heat-inactivated foetal bovine serum and 1% Penicillin-Streptomycin (Thermo Fisher Scientific) in a humidified 37°C incubator with 5% CO_2, as per our earlier reported protocol [42]. For high-$[K^+]_e$ treatment, cells were cultured in custom prepared high-$[K^+]_e$ RPMI 1640 medium containing isotonic 50 mM K^+, as described previously [9]. Experiments were performed in compliance with institutional guidelines and were approved by the Institutional Review Board of Nanyang Technological University Singapore (IRB-2018-05-034). Tumour samples of HCC and CRC were obtained from Tan Tock Seng Hospital, Singapore (DSRB#205-003).

4.2 | In Vitro Activation of T-Cells

PBL T-cells were activated by TCR engagement in vitro. Briefly, 1 μg/mL monoclonal anti-human CD3 (eBioscience) diluted in phosphate buffer saline (PBS) was coated on the wells of 12-well plates. After overnight incubation at 4°C, wells were washed with PBS. T-cells (1×10^6 cells in 500 μL medium/well) in RPMI 1640 containing physiological/normal 5 mM $[K^+]_e$ or treated in isotonic 50 mM high-$[K^+]_e$ medium were added into the wells. The medium was supplemented with 0.2 μg/mL monoclonal anti-human CD28 (eBioscience). Subsequently, cells were incubated in a cell culture incubator for 1–6 days, depending on specific treatment conditions/duration, and analysed.

4.3 | Flow-Cytometry Analysis

T-cell proliferation was determined by CellTrace Carboxy Fluorescein Succinimidyl Ester (CFSE) kit (Thermo Fisher Scientific) as per the manufacturer's protocol. Briefly, cells were resuspended in 1 mL serum-free RPMI 1640 supplemented with 5 μM CFSE and incubated at 37°C for 15 min. CFSE-labelled T-cells were added to anti-CD3-coated 24-well plates in 5 or 50 mM $[K^+]_e$ medium with the addition of 0.2 μg/mL anti-CD28. At defined time-points (24 h intervals), cells were stained with anti-CD3-BUV395, anti-CD4-BV650, anti-CD8-BV786 and 7-AAD-PE/Cy5.5 (live/dead staining, all from BD Biosciences). The proliferation of $CD4^+$ and $CD8^+$ T-cells was analysed by BD LSRFortessa X-20 Cell Analyzer. To determine T-cell differentiation into various subsets, cells were further stained with anti-CCR4-PE, anti-CXCR3-PE/Cy7, anti-CCR10-APC, anti-CCR6-BV421 (BioLegend), anti-CD127-PE-CF594 (Thermo Fisher Scientific), anti-CD25-PE, Fixable Viability Stain 510 (FVS510; viability dye for intracellular staining) and/or anti-FOXP3-R718 (BD Biosciences), as needed for specific experiments, and analysed by flow-cytometry. For certain experiments, to determine specific protein expression levels as indicated in corresponding figure legends, activated T-cells were stained with Mitotracker Red CMXROS, Mitotracker Green and CellROX Deep Red reagent (Thermo Fisher Scientific), 2-NBDG (MedchemExpress), anti-CD217(IL-17Ra)-APC, anti-LFA-1-PE/Cy7, anti-CD2-FITC, anti-ICOS-PE (BD Biosciences), anti-CD69-FITC, anti-CD3ζ-PE, anti-PD-1-PE, anti-LAG-3-BV421 (BioLegend), anti-CD28-PE (Assay Genie), anti-GLUT1-FITC and/or anti-GLUT4-FITC (Santa Cruz) and analysed by BD LSRFortessa X-20 Cell Analyzer.

4.4 | T-Cell Cytotoxicity Assay

T-cell cytotoxicity was determined using the breast cancer cell line MCF-7 and real-time monitoring of killing by the xCELLigence RTCA system (ACEA Biosciences). Briefly, MCF-7 cells (2.0×10^4 cells/well) were seeded in the wells of a RTCA E-plate 16 and incubated overnight. The next day, primary T-cells pre-activated using 1 μg/mL monoclonal anti-human CD3 and 20 ng/mL IL-2 were added to the well at an effector to target ratio of 15:1 in 5 or 50 mM $[K^+]_e$ medium. Subsequently, T-cell-mediated killing of MCF-7 cells was automatically recorded at 15 min intervals for up to 24 h by the xCELLigence RTCA system. Results in terms of baseline cell index were automatically generated by the system and presented.

4.5 | Glucose Uptake Assay

Intracellular glucose levels in T-cells were assessed using the Promega Glucose Uptake-Glo Assay kit in accordance with manufacturer's instructions. Briefly, T-cells (3×10^6 cells/mL) were activated with anti-CD3/28 antibodies in 5 or 50 mM $[K^+]_e$ medium for 24 h and washed with PBS. Activated T-cells were incubated with 1 mM 2-deoxyglucose (2-DG) in PBS for 10 min at room temperature and transferred into the wells of a white luminometer 96-well plate (Thermo Fisher Scientific). The stop

EOS, FOXO3, FOXO1, and c-Rel mRNA transcripts in activated T-cells were determined by RT-qPCR. (I) A schematic of the visualization of the outer and core zones of HCC/CRC tumours. (J) Relative % of Th1 and Th2 subsets (relative to $CD4^+$ T-cells) in HCC (hollow data points) and CRC (solid blue data points) tumour core versus the outer zones were quantified by flow-cytometry and point biserial correlation analysis was performed (lines in red). Positive or negative values in red are point biserial correlation coefficients (r_{pb}). (K) Relative % of $FOXP3^+CD25^+CD127^{(low)}$ population (relative to $CD4^+$ T-cells) in HCC/CRC tumours versus peripheral blood were quantified by flow-cytometry. Densitometry values indicated in the blots (D, F, and G), normalized based on control T-cells activated in 5 mM $[K^+]_e$ relative to actin or GAPDH, are mean of at least three independent experiments using PBL T-cells from at least three different donors. Full-length blots are provided in the Supporting Information section. Each data point in the graphs represents PBL T-cells from an individual donor, and bar graphs show mean ± SEM. A two-tailed paired *t*-test was used for statistical analysis of the results (*$p < 0.05$; **$p < 0.01$; ***$p < 0.001$). MFI, mean fluorescence intensities.

and neutralization buffers were sequentially added with gentle shaking between each addition. The 2-DG-6-phosphate (2DG6P) detection reagent, prepared according to the manufacturer's instructions, was added to the wells and incubated for 30 min at room temperature with gentle shaking. Luminescence readouts were recorded with an integration time of 1 s on the SkanIt Varioskan LUX Multimode multiple reader (Thermo Fisher Scientific).

4.6 | Glutamine Uptake Assay

Intracellular glutamine levels in T-cells were assessed using Promega Glutamine/Glutamate-Glo Assay kit in accordance with manufacturer's instructions. Briefly, T-cells (3×10^6 cells/mL) were activated with anti-CD3/28 antibodies in 5 or 50 mM $[K^+]_e$ medium for 24 h and washed with 1× PBS. Activated T-cells were resuspended in PBS and lysed with the inactivation solution I (0.3 N HCl). The lysates were transferred into the wells of a white luminometer 96-well plate (Thermo Fisher Scientific) and shaken for 5 min. Tris solution I (600 mM Tris, pH 8.5) was then added to the wells and shaken for an additional 1 min. The glutaminase assay buffer was added to the wells and shaken for 1 min before the plate was incubated for 30 min at room temperature. The glutamate detection reagent, supplemented with other components, was subsequently added to the wells and shaken for 1 min followed by 1 h incubation at room temperature. Luminescence readouts were recorded with an integration time of 1 s on the SkanIt Varioskan LUX Multimode multiple reader (Thermo Fisher Scientific).

4.7 | Metabolomics Analysis

PBL T-cells collected from four different donors were activated in either 5 or 50 mM $[K^+]_e$ medium for 6 days. Cells were washed twice with 150 mM ice-cold NaCl, harvested and centrifuged at $3000 \times g$ for 5 min at 4°C prior to storage at −80°C for further analysis. Cellular metabolites (both aqueous and liquid extracts) were extracted using a previously reported two-phase extraction protocol [43]. Briefly, lipid metabolites were separated from aqueous species using methanol:chloroform:3.8 mM tricine solution (1:1:0.5, v/v). An Acquity UPLC system (Waters) in tandem with a Q Exactive mass spectrometer (Thermo Fisher Scientific) was used to analyse aqueous extracts. A C18 reversed phase column (2.1×100 mm^2, 1.7 µm, Acquity UPLC HSS T3 column, Waters) and the following two solvents were used: solvent A—water with 0.1% formic acid (Merck) and solvent B—methanol (Fisher Scientific, optima grade) with 0.1% formic acid. The following column equilibration step was used (UPLC program): 0.5 min in 0.1% solvent B followed by gradient steps of increasing amounts of solvent B from 0.1% to 50% over 8 min duration before being held at 98% for 3 min. After these steps, column was washed for 3 min with 98% acetonitrile (LiChrosolv grade, Merck) containing 0.1% formic acid and finally equilibrated at 0.1% B for 1.5 min. The flow-rate and the column temperature were kept at 0.4 mL/min and 30°C, respectively. Electrospray ionization was performed in both positive and negative modes with a mass range of 70–1050 m/z at a resolution of 70,000. Sheath and auxiliary gas flow was kept at 30.0 and 20.0 (arbitrary units), respectively, with 400°C capillary temperature and 1.5 and 1.25 kV spray voltage for positive and negative mode ionization, respectively. An Acquity UPLC system coupled to a Synapt G2-Si mass spectrometer (Waters) was used to analyse lipid extracts. A C18 UPLC column (1.0×50 mm^2, 1.7 µm, Acquity UPLC CSH column, Waters) and the following two solvents were used: solvent A—methanol:acetonitrile:water (2:2:1 v/v) containing 0.1% acetic acid (Merck) and 0.025% ammonia solution (VWR), and solvent B—isopropanol containing 0.1% acetic acid and 0.025% ammonia solution. The following UPLC programme was used: The gradient was initially held for 1 min at 0.1 mL/min in 1% solvent B. Thereafter, solvent B was increased to 82.5% over 9 min and further to 99% for a 5 min wash at 0.15 mL/min. The column was re-equilibrated in 1% solvent B for 2 min at 0.1 mL/min. The column was maintained at 45°C. Electrospray ionization was carried out in both positive and negative modes with a mass range of 100–1800 m/z at a resolution of 10,000. Cone and desolvation gas flows were kept at 40.0 and 600.0 (L/h), respectively, at 600°C with capillary voltages of 2.0 and 1.0 kV, respectively, for positive and negative mode ionization. The quality control sample comprised equal aliquots of each sample and was run at regular intervals during the batch LC–MS runs. The raw LC/MS data were processed using XCMS, a widely used R package for peak finding, and quality control samples were used to adjust for instrumental drift. Putative metabolite identities were assigned based on detected mass peaks by matching the respective masses with the KEGG and Human Metabolome Database (<10 ppm error). The identities of selected metabolites of interest were confirmed on the basis of metabolite standards. Identified metabolites that attained both p values <0.05 (Welch's t-test) and showed at least 50% increased or decreased relative abundance in all four biological replicates were further analysed. The metabolome mapping and gene–metabolite interaction networks were constructed using MetaboAnalyst 5.0.

4.8 | Real-Time Quantitative PCR (RT-qPCR)

At the end of experimental treatments, as indicated in respective figure legends, T-cells were harvested, centrifuged at $5000 \times g$ for 5 min, and RNA was isolated using RNeasy Mini Kit (Qiagen). The concentrations of isolated RNA samples were determined using Nanodrop 2000 Spectrophotometer. Complementary DNA (cDNA) was generated from 1 µg of RNA samples using M0MuLV Reverse Transcriptase (New England Biolabs), oligo DT primers (Promega) and the Applied Biosystems thermocycler. qPCR was performed using PowerUp SYBR Master Mix (Thermo Fisher Scientific) with thermal cycles as follows: 50°C for 2 min > 95°C for 2 min > (95°C for 15 s followed by 60°C for 1 min) × 40 cycles > 95°C for 15 s > 60°C for 1 min > 95°C for 15 s.

4.9 | Enzyme-Linked Immunosorbent Assay (ELISA)

The amounts of secreted cytokines (IL-4, IFN-γ, IL-17A) were determined using DIY ELISA Kits (Assay Genie) and human Ready-SET-Go ELISA kits (Thermo Fisher Scientific). Absorbance readings were recorded at 450 and 570 nm using Varioskan LUX multimode microplate reader.

4.10 | Western Immunoblotting

At the end of experimental treatments, as indicated in respective figure legends, T-cells were harvested by centrifugation at 5000 × *g* for 5 min, and lysed in lysis buffer supplemented with Pierce Protease Inhibitor, EDTA-free and PhosSTOP (Merck). Cellular lysates were clarified by centrifugation at 13,000 × *g* for 10 min at 4°C. Bradford protein assay was performed to determine the amounts of proteins in cellular lysates. Laemmli sample buffer (Bio-Rad) was added to the lysates, followed by heating of the samples at 95°C for 5 min before gel loading. Protein samples were resolved on SDS–PAGE and then transferred onto PVDF membranes. Subsequently, membranes were blocked with 5% Blotto (Bio-Rad) for 1 h before incubating with specific primary antibodies overnight at 4°C. After washing three times with an interval of 5 min each using tris-buffered saline containing 0.1% Tween-20, blots were probed with secondary antibodies of either anti-rabbit or anti-mouse HRP conjugate (Jackson ImmunoResearch) and incubated for 1 h at room temperature. Blots were developed using a chemiluminescent substrate and imaged by a Bio-Rad ChemiDoc system. Protein bands were quantified using densitometric analysis with the help of the ImageJ software.

5 | GeoMx Digital Spatial Profiler (DSP) Whole Transcriptome Workflow

HCC/CRC tumour tissue sections ($n = 8$) were resected from the core to the outer peripheral zone of tumours. The sections (5 μm) were used for GeoMx DSP whole transcriptome sequencing (Nanostring). The slides were stained with the following panel of morphology markers: CD3 for T-cell, Syto 83 nuclear stain and pan cytokeratin. Subsequently, slides were treated with GeoMx DSP oligo-conjugated RNA detection probes in accordance with the manufacturer's instructions. A total of 12 area of interests (AOIs; up to 660 × 785 μm^2) were selected for each tumour tissue section. The AOIs were then exposed to ultraviolet light to cleave the RNA tags that were hybridized to GeoMx unique hybridization barcodes, tagged with specific RNA target identification sequences during library preparation. The oligonucleotides were imported into the GeoMx platform and overlaid with the section images and AOI selection for spatially resolved RNA expression.

5.1 | Statistical Analysis

All the experiments were replicated at least three times. Depending on specific experiments, comparison between two groups was made by paired student's *t*-test and comparisons of multiple groups within a single experiment were made by one-way ANOVA. Prism 9.5.0 (GraphPad) was used to make the graphs and statistical analyses.

Author Contributions

Navin Kumar Verma and K. George Chandy conceived the project and designed experiments. Brandon Han Siang Wong, Zhi Sheng Poh, James Tan Chia Wei and Kottaiswamy Amuthavalli performed T-cell experiments and functional analysis. Ying Swan Ho, Shuwen Chen, Shi Ya Mak and Xuezhi Bi performed metabolomics analysis. Vishalkumar G. Shelat collected patient tumour samples and contributed to the methodology. Brandon Han Siang Wong and Navin Kumar Verma wrote the original draft of the manuscript. Funding acquisition was realized by Navin Kumar Verma and Xuezhi Bi. Navin Kumar Verma, Richard D. Webster, Vishalkumar G. Shelat and K. George Chandy supervised the project. All authors provided a discussion, contributed to writing and agreed to the final version.

Acknowledgements

This research was supported, in part, by the Singapore Ministry of Education (MOE) under its MOE Academic Research Fund (AcRF) Tier 2 Grant (MOE2017-T2-2-004), AcRF Tier 1 Grant (2020-T1-001-062), and the National Research Foundation Singapore under its Open Fund Large Collaborative Grant (OFLCG18May-0028) and administered by the Singapore Ministry of Health's National Medical Research Council (NMRC). Navin Kumar Verma was a recipient of these grants. The metabolomics analysis was supported by Xuezhi Bi through the Agency for Science, Technology and Research (A*STAR), Singapore. Brandon Han Siang Wong and Zhi Sheng Poh are recipients of PhD fellowships from HealthTech NTU and Lee Kong Chian School of Medicine, Nanyang Technological University Singapore.

Ethics Statement

Experiments utilizing human peripheral blood samples were performed in accordance with institutional guidelines and were approved by the Institutional Review Board of Nanyang Technological University Singapore (IRB-2018-05-034). Tumour samples of HCC and CRC were obtained after written consent and as per the approved Domain Specific Review Board guidelines (DSRB#205-003). Some of the figure panels contain elements from Biorender (https://biorender.com).

Conflicts of Interest

The authors declare no conflicts of interest.

Data Availability Statement

The data that support the findings of this study are available from the corresponding author upon reasonable request.

Peer Review

The peer review history for this article is available at https://publons.com/publon/10.1002/eji.202451440.

References

1. P. S. Hegde and D. S. Chen, "Top 10 Challenges in Cancer Immunotherapy," *Immunity* 52 (2020): 17–35.

2. J. Varadé, S. Magadán, and A. González-Fernández, "Human Immunology and Immunotherapy: Main Achievements and Challenges," *Cellular & Molecular Immunology* 18 (2021): 805–828.

3. D. Gumber and L. D. Wang, "Improving CAR-T Immunotherapy: Overcoming the Challenges of T Cell Exhaustion," *EBioMedicine* 77 (2022): 103941.

4. N. K. Verma, B. H. S. Wong, Z. S. Poh, et al., "Obstacles for T-Lymphocytes in the Tumour Microenvironment: Therapeutic Challenges, Advances and Opportunities Beyond Immune Checkpoint," *EBioMedicine* 83 (2022): 104216.

5. Y. Tokumaru, L. Le, M. Oshi, et al., "Association of Th2 High Tumors With Aggressive Features of Breast Cancer," *Journal of Clinical Oncology* 38, no. S15 (2020): e12584.

6. L. De Monte, M. Reni, E. Tassi, et al., "Intratumor T Helper Type 2 Cell Infiltrate Correlates With Cancer-Associated Fibroblast Thymic Stromal Lymphopoietin Production and Reduced Survival in Pancreatic Cancer," *Journal of Experimental Medicine* 208 (2011): 469–478.

7. P. Winnand, K. O. Boernsen, M. Ooms, et al., "The Role of Potassium in Depth Profiling of the Tumor Border in Bone-Invasive Oral Cancer Using Laser-Induced Breakdown Spectroscopy (LIBS): A Pilot Study," *Journal of Cancer Research and Clinical Oncology* 149 (2023): 16635–16645.

8. R. Eil, S. K. Vodnala, D. Clever, et al., "Ionic Immune Suppression Within the Tumour Microenvironment Limits T Cell Effector Function," *Nature* 537 (2016): 539–543.

9. S. T. Ong, A. S. Ng, X. R. Ng, et al., "Extracellular K^+ Dampens T Cell Functions: Implications for Immune Suppression in the Tumor Microenvironment," *Bioelectricity* 1 (2019): 169–179.

10. T. L. Stephen, B. S. Wilson, and T. M. Laufer, "Subcellular Distribution of Lck During CD4 T-Cell Maturation in the Thymic Medulla Regulates the T-Cell Activation Threshold," *Proceedings of the National Academy of Sciences of the United States of America* 109, no. 19 (2012): 7415–7420.

11. I. Evnouchidou, V. Caillens, D. Koumantou, and L. Saveanu, "The Role of Endocytic Trafficking in Antigen T Cell Receptor Activation," *Biomedical Journal* 45 (2022): 310–320.

12. R. Ouchida, S. Yamasaki, M. Hikida, et al., "A Lysosomal Protein Negatively Regulates Surface T Cell Antigen Receptor Expression by Promoting CD3zeta-Chain Degradation," *Immunity* 29 (2008): 33–43.

13. P. P. Sun, S. X. Liao, P. Sang, M. M. Liu, and J. B. Yang, "Lysosomal Transmembrane Protein 5: Impact on Immune Cell Function and Implications for Immune-Related Deficiencies," *Heliyon* 10 (2024): e36705.

14. Y. Mita, M. Y. Kimura, K. Hayashizaki, et al., "Crucial Role of CD69 in Anti-Tumor Immunity Through Regulating the Exhaustion of Tumor-Infiltrating T Cells," *International Immunology* 30 (2018): 559–567.

15. R. Koyama-Nasu, Y. Wang, I. Hasegawa, Y. Endo, T. Nakayama, and M. Y. Kimura, "The Cellular and Molecular Basis of CD69 Function in Anti-Tumor Immunity," *International Immunology* 34 (2022): 555–561.

16. Y. Han, Q. Guo, M. Zhang, Z. Chen, and X. Cao, "$CD69^+CD4^+CD25^-$T Cells, a New Subset of Regulatory T Cells, Suppress T Cell Proliferation Through Membrane-Bound TGF-β1," *Journal of Immunology* 182 (2009): 111–120.

17. G. Soto-Heredero, G. Desdín-Micó, and M. Mittelbrunn, "Mitochondrial Dysfunction Defines T Cell Exhaustion," *Cell Metabolism* 33 (2021): 470–472.

18. J. A. Shyer, R. A. Flavell, and W. Bailis, "Metabolic Signaling in T Cells," *Cell Research* 30 (2020): 649–659.

19. S. K. Vodnala, R. Eil, R. J. Kishton, et al., "T Cell Stemness and Dysfunction in Tumors Are Triggered by a Common Mechanism," *Science* 363 (2019): eaau0135.

20. S. Dimeloe, A. V. Burgener, J. Grählert, and C. Hess, "T-Cell Metabolism Governing Activation, Proliferation and Differentiation; a Modular View," *Immunology* 150 (2017): 35–44.

21. P. J. Siska and J. C. Rathmell, "T Cell Metabolic Fitness in Antitumor Immunity," *Trends in Immunology* 36 (2015): 257–64.

22. I. R. Antony, B. H. S. Wong, D. Kelleher, and N. K. Verma, "Maladaptive T-Cell Metabolic Fitness in Autoimmune Diseases," *Cells* 12 (2023): 2541.

23. D. S. Thommen and T. N. Schmacher, "T Cell Dysfunction in Cancer," *Cancer Cell* 33 (2018): 547–562.

24. A. Chow, K. Perica, C. A. Klebanoff, and J. D. Wolchok "Clinical Implications of T Cell Exhaustion for Cancer Immunotherapy," *Nature Reviews Clinical oncology* 19 (2022): 775–790.

25. A. Alcover, B. Alarcón, and V. Di Bartolo, "Cell Biology of T Cell Receptor Expression and Regulation," *Annual Review of Immunology* 36 (2018): 103–125.

26. M. A. Linterman, A. E. Denton, D. P. Divekar, et al., "CD28 Expression Is Required After T Cell Priming for Helper T Cell Responses and Protective Immunity to Infection," *Elife* 3 (2014): e03180.

27. D. Langenhorst, S. Haack, S. Göb, et al., "CD28 Costimulation of T Helper 1 Cells Enhances Cytokine Release In Vivo," *Frontiers in Immunology* 9 (2018): 1060.

28. J. J. Butler, J. S. Mader, C. L. Watson, H. Zhang, J. Blay, and D. W. Hoskin, "Adenosine Inhibits Activation-Induced T Cell Expression of CD2 and CD28 Co-Stimulatory Molecules: Role of Interleukin-2 and Cyclic AMP Signaling Pathways," *Journal of Cellular Biochemistry* 89 (2003): 975–991.

29. E. Hui, J. Cheung, J. Zhu, et al., "T Cell Costimulatory Receptor CD28 Is a Primary Target for PD-1-Mediated Inhibition," *Science* 355 (2017): 1428–1433.

30. R. Mizuno, D. Sugiura, K. Shimizu, et al., "PD-1 Primarily Targets TCR Signal in the Inhibition of Functional T Cell Activation," *Frontiers in Immunology* 10 (2019): 630.

31. E. J. Wherry and M. Kurachi, "Molecular and Cellular Insights Into T Cell Exhaustion," *Nature Reviews Immunology* 15 (2015): 486–499.

32. L. P. Andrews, S. C. Butler, J. Cui, et al., "LAG-3 and PD-1 Synergize on $CD8^+$ T Cells to Drive T Cell Exhaustion and Hinder Autocrine IFN-γ-Dependent Anti-Tumor Immunity," *Cell* 187 (2024): 4355–4372.

33. A. R. Cillo, C. Cardello, F. Shan, et al., "Blockade of LAG-3 and PD-1 Leads to Co-Expression of Cytotoxic and Exhaustion Gene Modules in $CD8^+$ T Cells to Promote Antitumor Immunity," *Cell* 187 (2024): 4373–4388.

34. C. Collier, K. Wucherer, M. McWhorter, et al., "Intracellular K^+ Limits T-Cell Exhaustion and Preserves Antitumor Function," *Cancer Immunology Research* 12 (2024): 36–47.

35. M. Chirra, H. S. Newton, V. S. Gawali, T. M. Wise-Draper, A. A. Chimote, and L. Conforti, "How the Potassium Channel Response of T Lymphocytes to the Tumor Microenvironment Shapes Antitumor Immunity," *Cancers* 14 (2022): 3564.

36. J. Blagih, F. Coulombe, E. E. Vincent, et al., "The Energy Sensor AMPK Regulates T Cell Metabolic Adaptation and Effector Responses In Vivo," *Immunity* 42 (2015): 41–54.

37. G. C. Preston, L. V. Sinclair, A. Kaskar, et al., "Single Cell Tuning of Myc Expression by Antigen Receptor Signal Strength and Interleukin-2 in T Lymphocytes," *Embo Journal* 34 (2015): 2008–2024.

38. S. Liu, S. Liao, L. Liang, J. Deng, and Y. Zhou, "The Relationship Between $CD4^+$ T Cell Glycolysis and Their Functions," *Trends in Endocrinology and Metabolism* 34 (2023): 345–360.

39. J. Ly, M. Lagman, T. Saing, et al., "Liposomal Glutathione Supplementation Restores Th1 Cytokine Response to *Mycobacterium tuberculosis* Infection in HIV-Infected Individuals," *Journal of Interferon & Cytokine Research* 35 (2015): 875–887.

40. M. Johansson, D. G. Denardo, and L. M. Coussens, "Polarized Immune Responses Differentially Regulate Cancer Development," *Immunological Reviews* 222 (2008): 145–154.

41. M. Pandit, M. Timilshina, Y. Gu, et al., "AMPK Suppresses Th2 Cell Responses by Repressing mTORC2," *Experimental & Molecular Medicine* 54, no. 8 (2022): 1214–1224.

42. A. Kizhakeyil, S. T. Ong, M. H. U. T. Fazil, M. L. S. Chalasani, P. Prasannan, and N. K. Verma, "Isolation of Human Peripheral Blood T-Hymphocytes," *Methods in Molecular Biology* 1930 (2019): 11–17.

43. F. N. K. Yusufi, M. Lakshmanan, Y. S. Ho, et al., "Mammalian Systems Biotechnology Reveals Global Cellular Adaptations in a Recombinant CHO Cell Line," *Cell Systems* 4 (2017): 530–542.e6.

Supporting Information

Additional supporting information can be found online in the Supporting Information section.